Local conformations and heterogeneities in structures and dynamics of isotactic polypropylene adsorbed onto carbon fiber

Zhixing Huang^{1,#}, Yashasvi Bajaj^{1,#}, Jan-Michael Y. Carrillo², Yohei Nakanishi³, Kiminori Uchida³, Kazuki Mita^{3,4}, Takeshi Yamada⁴, Tsukasa Miyazaki⁴, Bobby G. Sumpter², Maya Endoh^{1,*}, Tadanori Koga^{1,*}

¹Department of Materials Science and Chemical Engineering, Stony Brook University, Stony Brook, New York, 11794-2275

²Center for Nanophase Materials Sciences, Oak Ridge National Laboratory, Oak Ridge, Tennessee, 37831

³Mitsui Chemicals Inc., 580-32 Nagaura, Sodegaura, Chiba 299-0265, Japan

⁴Neutron Science and Technology Center, Comprehensive Research Organization for Science and Society (CROSS), Tokai, Ibaraki 319-1106, Japan

*Corresponding authors: tadanori.koga@stonybrook.edu (T. K.); maya.koga@stonybrook.edu (M.E.)

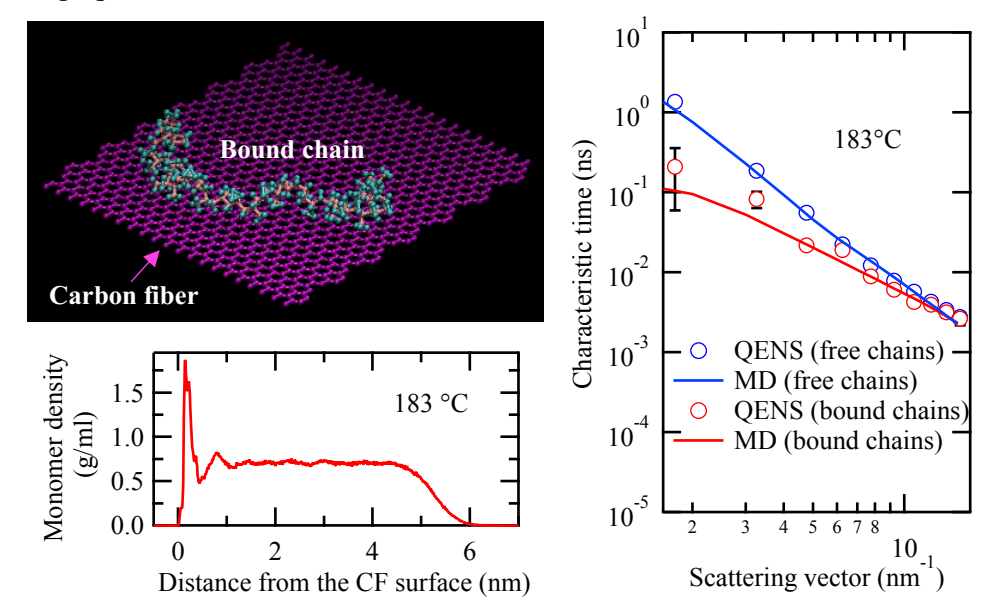
Keywords: bound polymer, quasi-elastic neutron scattering, atomistic molecular dynamics simulations, chain packing, interfacial structures and dynamics

[#]Equal contributions to the first authorship

Abstract

Carbon fiber (CF) reinforced polymers (CFRPs) have experienced widespread use in various industries. One of the most important parameters that controls the macroscopic property of CFRPs is the interface between a polymer matrix and CF. There is growing evidence to suggest the formation of a bound polymer layer (BPL), i.e., polymer chains that physically adsorb on a filler surface. However, this interface is always in contact with the thicker part of a polymer matrix, rendering its understanding a difficult task. Therein, we use CF-reinforced isotactic polypropylene (iPP) as a rational CFRP. To characterize the BPL on the CF surface, we extracted it from the CFRP using solvent-rinsing with p-xylene. The physical and thermal properties of the BPL were characterized by differential scanning calorimetry and thermogravimetric analysis, while its microscopic structures and dynamics were probed by small-angle neutron scattering and quasi-elastic neutron scattering (QENS) techniques. Subsequently, we employed atomistic molecular dynamics (MD) simulations to complement the QENS results above the bulk melting temperature and reveal details that were experimentally inaccessible. We observed that the degree of crystallinity of the BPL was quite lower than the bulk, while the melting temperature of the BPL remained the same as the bulks. Within the given length and time scales probed by QENS and MD, we also observed that most of the bound chains were mobile, with the formation of a high-density region (less than 1 nm in thickness) near the CF surface. The segmental dynamics of the bound chains probed by both QENS and MD were also much faster than those of the free chains, possibly due to the presence of a free surface region at the topmost surface of the BPL. Furthermore, the MD results demonstrated that the backbone chains and side groups lie nearly flat on the CF surface, which is the driving force for the flattening process of the iPP BPL to overcome the conformational entropy loss in the total free energy.

TOC graphic



1. Introduction

Polymer nanocomposites continue to generate remarkable scientific and applied interest, given their structurally, dynamically, and mechanically beneficial behaviors that involve fundamental polymer and colloid science aspects [1, 2]. Furthermore, carbon fiber (CF) reinforced polymers (CFRPs) are used extensively in ground and air transportation, construction, and sporting goods industry [3-7] due to their superior mechanical properties such as high tensile strength, high modulus, and remarkable wear resistance [3, 8]. It is especially important that CFRPs can achieve these excellent properties together with light weight. The light weight characteristic results in improved fuel efficiency for automobiles and aircrafts, which, in turn, contributes to the realization of a carbon-neutral society.

Among the most important parameters that control the macroscopic properties of CFRPs is the interface between a polymer matrix and CF [9, 10]. There is growing evidence to suggest the formation of a bound polymer layer (BPL), i.e., polymer chains that physically adsorb on the filler surfaces such as carbon black [11-16] and silica [17, 18]. The BPL can interact with a matrix polymer and concurrently bridge neighboring fillers. The thickness of the BPL is commensurate with the radius of gyration (R_g) of bound polymer chains [19-27]. The BPL itself is made up of three types of segment sequences [28]: "trains" (fully adsorbed segments), "loops" (sequences of free segments connecting successive trains), and "tails" (non-adsorbed chain ends). Bound polymer chains also exhibit a more elastic mechanical property [29-31] and higher glass transition temperature (T_g) [32, 33] than the bulks. At high filler loadings where the interparticle distance between neighboring fillers is on the order of the BPL thickness, bound chains begin to form "doubly adsorbed" polymer segments, or polymer bridges [34-36] between neighboring fillers. This results in the formation of a filler network. Among several factors contributing to mechanical property enhancement, this filler network contributes the most [29, 32, 35, 37-46]. On the other hand, the majority of the BPL is *not* in bridges, but rather at the level of individual chains in tails and large loops. The tails entangle (or large loops interdigitate) with free matrix chains [47-50], acting as "connectors" [51, 52] between a filler and a matrix polymer. Sokolov and co-workers also indicated that the flexibility of the BPL enhances the mechanical property of polymer nanocomposites [53].

In this paper, isotactic polypropylene (iPP), a widely utilized commodity polyolefin, mixed with CF is our target CFRP. Due to experimental constraints, molecular dynamics simulations are alternatively used to shed light on the buried structures and dynamics of polymer/graphite hybrid materials [54-59]. To expose the BPL to the air, we use an established solvent-based method [21, 48, 60] and characterize its physical and thermal properties using differential scanning calorimetry and thermogravimetric analysis. Moreover, we unravel the microscopic structures and dynamics of the BPL above the melting temperature with neutron scattering and spectroscopy techniques. Motivated by previous work, we then employ atomistic molecular dynamics (MD) simulations to complement the neutron scattering and spectroscopy results and reveal more detailed structural and dynamical features. Herein, the integrated experimental and computation study shows the unique "flattening" process of the backbone and side groups of the iPP BPL, as well as the resultant heterogeneities in buried structures and dynamics, both critical parameters to better understand the molecular mechanisms behind macroscopic property enhancements of the model CFRP.

2. Experimental Section

2.1 Materials

iPP (average molecular weight $(M_w) = 250,000$ g/mol, Cat. No. 427888, MilliporeSigma, St. Louis, USA) and CF (average diameter = 7 ± 1 µm, average length = 10 ± 1 mm, Mitsubishi Chemical Corp.) were used. The error bars used in this paper represent ± 1 standard deviation unless otherwise noted. Para-xylene (p-xylene, > 98%, FUJIFILM Wako Pure Chemical Corporation, Osaka, Japan), deuterated p-xylene (d-xylene, MilliporeSigma, Product No. 175927), and acetone (>99.5%, FUJIFILM Wako) were used as received.

The preparation of the BPL on the CF filler is schematically illustrated in Fig. 1. CFs were first cleaned by acetone in an ultrasonic bath for 20 min, three times, and then blended into an iPP matrix by compression molding at 200 °C, using a loading force of 10 MPa, for 5 min, and cooled at 20 °C for 3 min. Next, the BPL layer formed on CF surfaces (hereafter assigned as "the BPL-coated CF") was then exposed by heated p-xylene at about 150 °C (a good solvent) multiple times and removed of unadsorbed chains. The details of the solvent rinsing process

have been described elsewhere [21, 48, 60]. After rinsing and subsequent acetone replacement, the BPL-coated CF fillers were placed in a vacuum oven at room temperature overnight to evaporate all residue solvent molecules.

2.2 Techniques

Thermogravimetric Analysis (TGA)

The thermal properties of the BPL-coated CF fillers and neat iPP were characterized by using thermogravimetry (TGA Q5000IR, TA instruments, New Castle, DE, USA). At the same time, we also characterized the bare CF as a control. The instrument was calibrated by using nickel and cobalt before measurements. 10 mg of each sample was used for TGA measurements. The heating rate of 10 °C/min was used for the temperature ramp from room temperature to 800 °C. The TGA curves were analyzed as percentage weight loss as a function of temperature. As will

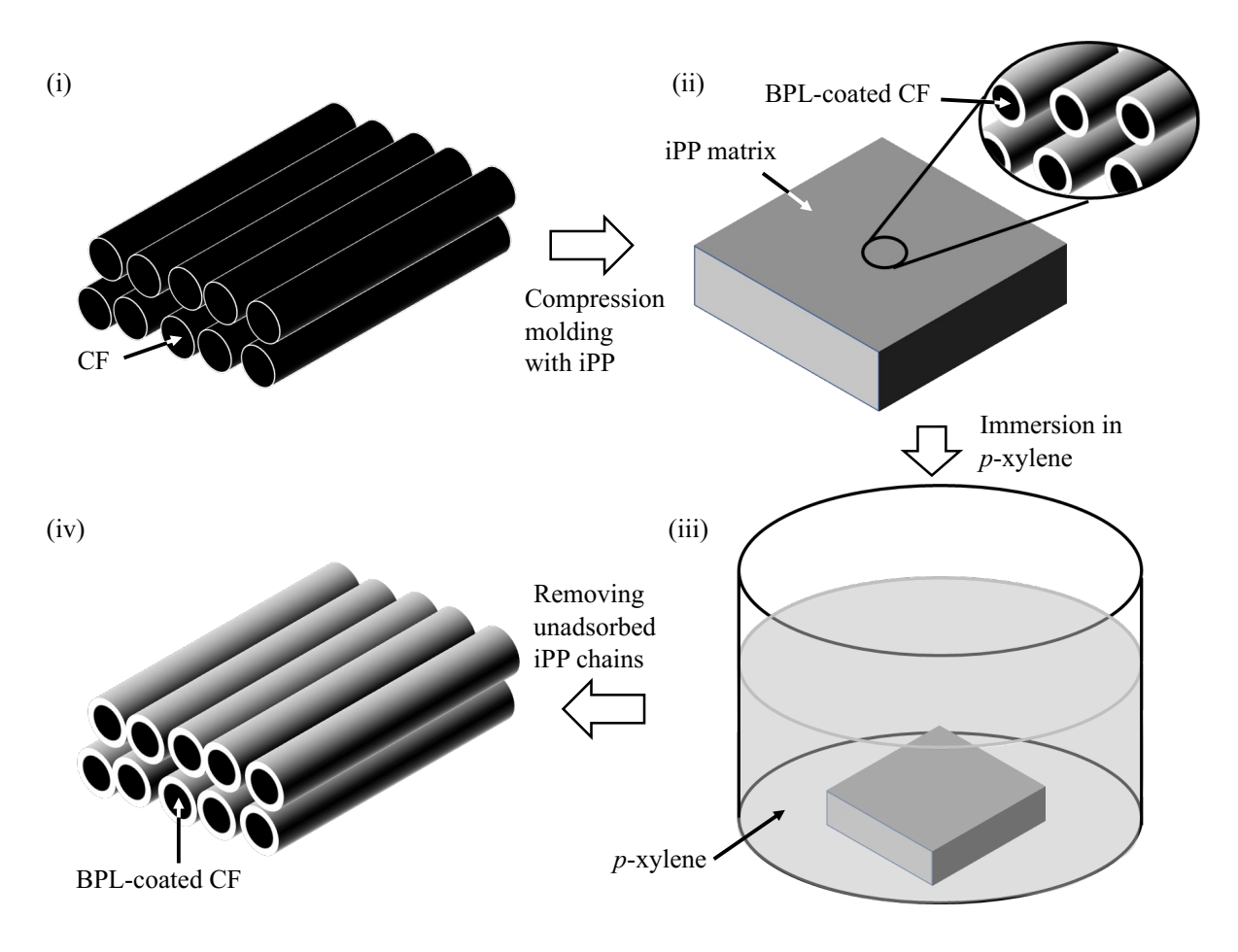


Fig. 1. Schematic diagram of the sample preparation (not drawn to scale) for the TGA, DSC, SANS, and QENS experiments.

be discussed later, the weight fraction of the bound layer in the BPL-coated CF was 0.5 %.

Differential Scanning Calorimetry (DSC)

The melting temperatures of the BPL-coated CF fillers and neat iPP were characterized by using DSC instruments (Discovery DSC2500 and Q2000, TA instruments). All experiments were conducted in a nitrogen environment with a flow rate of 50 mL/min. The heating rate was 10 °C/min. The respective sample was sealed in an aluminum pan with a weight of around 5 mg. The apparatus was calibrated by indium, tin, and lead before measurements.

Small Angle Neutron Scattering (SANS)

As previously reported, we have established SANS techniques to identify the structural and dynamical properties of the BPL composed of polybutadiene on carbon black fillers dispersed in a good solvent [21], polymer solutions [25], and a polymer melt [48]. Here we used the same contrast-matched SANS using deuterated p-xylene (d-xylene, with the scattering length density (SLD) of 5.9×10^{-4} nm⁻²) to characterize the thickness of the iPP BPL on the CF (SLD = 5.1×10^{-4} nm⁻²) surface at room temperature. While the solubility parameter of the bulk iPP is 8.2 (cal/cm³) $^{1/2}$, which is close to that of d-xylene, 8.75 (cal/cm³) $^{1/2}$ at 25 °C [61], the dissolution temperature of iPP in p-xylene, where crystallites acting as "crosslinks" in the polymer are melted, is 102 °C [61]. Hence, p-xylene or d-xylene at room temperature behaves like a poor solvent, as will be discussed later. The measurements were carried out at the SANS beamline QUOKKA [62] at the Australian Nuclear Science and Technology Organization (ANSTO, Lucas Heights, Sydney, New South Wales, Australia) at 8.0 m sample-detector distance with a 0.6 nm wavelength. The scattering intensity was measured as a function of scattering vector, q = $4\pi \sin\theta/\lambda$, where 2θ represents the scattering angle and λ is the wavelength of the incident neutron beam. We also measured the SANS data for d-xylene and CF for the background corrections. The SANS data reduction and analysis were performed by using the program developed by the NIST Center for Neutron Research (NCNR) [63].

Quasi-elastic neutron scattering (QENS) experiments

QENS measurements, which provide the spatial (sub-nm to 1 nm) and temporal (10 ps to 1 ns) information, were conducted at a time-of-flight near backscattering spectrometer BL02-DNA [64] at the Materials and Life Science Experimental Facility in Japan Proton Accelerator Research Complex (J-PARC, Tokai, Japan) with an energy resolution of 3.6 μ eV and measured energy transfer range from $\Delta E = -40 \,\mu$ eV to $100 \,\mu$ eV. It should be noted that the contributions to the total scattering cross section from the CF fillers (i.e., coherent scattering) and the iPP bound chains (i.e., incoherent scattering) in the BPL-coated CF fillers was estimated to be 88 and 11 %, respectively (Table S1 of Supplementary Data). However, we confirmed that the QENS profiles of the bare CF at the two temperatures were almost identical to that of the resolution function, indicating the lack of QENS (Fig. S1 of the Supplementary Data). Hence, it is reasonable to conclude that the quasi-elastic scattering originates mostly from the self-motion of H atoms through the energy change of the scattered neutrons and allows us to calculate the dynamic incoherent structure factor, S(q, E) or $S(q, \omega)$ ($\omega = \Delta E/h$, where h is the Planck's constant and ω is the angular frequency).

Data were recorded in the q-range from 1 to 19 nm⁻¹, and the instrument resolution function was collected by measuring the sample at T = -263.15 °C (i.e., 10 K), where the sample was expected to be immobile, giving rise to complete elastic scattering. The QENS data analysis was performed by using the DAVE software package [65]. The BPL-coated CF fillers, bare CF fillers, and neat iPP were measured for QENS. The fiber samples (i.e., the BPL-coated CF fillers and bare CF fillers) and the neat iPP sample with a 0.1-mm thickness were put into an aluminum cylinder cell (having an inner diameter of 14 mm and a height of 40 mm) separately. We chose the two different temperatures (183 °C and 220 °C), both of which are above the bulk melting temperature, for QENS experiments.

In this paper, instead of analyzing $S(q, \omega)$, we computed the intermediate scattering function, I(q,t), by Fourier transform of the experimental data. The details will be discussed later. The relationship between $S(q,\omega)$ and I(q,t) is as follows:

$$S(q,\omega) = \frac{1}{2\pi} \int I(q,t) \exp(-i\omega t) dt, (1)$$

with

$$I(q,t) = \frac{1}{N_H} \left\langle \sum_{i}^{N_H} e^{i\vec{q} \cdot (\vec{r_i}(t) - \vec{r_i}(0))} \right\rangle, (2)$$

where $\vec{r_i}(t)$ is treated as the location of the i_{th} hydrogen atom after an elapsed time of t from its original location $\vec{r_i}(0)$ and N_H as the total number of hydrogen atoms.

Molecular dynamics (MD) simulations

We performed atomistic MD simulations to study the structures and dynamics of two systems: (i) iPP chains adsorbed on a CF surface and (ii) neat iPP free chains at $T > T_m$, where the temperature conditions of 183 °C and 220 °C were applied to both systems. According to a previous paper, the number of backbone bonds in a segment for iPP is about 5 [66]. Namely, the one Kuhn segment consists of three repeat units $(n, (C_3H_6)_n)$. We first studied the effect of n on the resultant equilibrium structures and dynamics by changing n from 6 to 45 and confirmed that n = 30 is the threshold above which the relaxation times are identical within error bars (Fig. S2 of the Supplementary Data). Therefore, we used n = 30 for both systems in this study. We also added a 'vacuum layer' unique to system (i), defined by a region of an empty space above a bound layer and below the CF surface. The number of iPP molecules (120) in system (i) was chosen together with the cross-sectional area of the simulation box. With this, we mimicked the thickness of the bound layer in MD simulations to that of our experiments, allowing us to approximate the partitioning of H atoms that are bound to CF and those that are suspended in the vacuum-film interface. In system (i), the CF surface was modeled as graphite with 1108 hexagonal unit cells, containing 52 in the x-axis, 60 in the y-axis, and 996 in the zaxis with the unit cell of a = 2.456 Å, b = 2.456 Å, c = 6.696 Å, $\alpha = 90^{\circ}$, $\beta = 90^{\circ}$, and $\gamma =$ 120°. The crystal structure information was obtained from the American Mineralogist Crystal Structure Database [67].

AVOGADRO software [68] was used to construct individual mol2 and pdb files of molecules and fix iPP root methyl group carbon atoms to approximate an isotactic stereoconfiguration. The methyl group hydrogen atoms were still allowed to move freely. The forcefield used was the generalized AMBER force field (GAFF) [69] and partial charges were derived from AM1BCC routine in Antechamber, a utility included in the AMBER software

package. The total energy potential energy in GAFF (U_{tot}) can be described as

$$\begin{split} U_{tot} &= \sum_{bonds} k_{bond} \left(r - r_{eq}\right)^2 + \sum_{angles} k_{angle} \left(\theta - \theta_{eq}\right)^2 + \sum_{dihedrals} k_{dihedral} \left[1 + dcos(n\phi)\right] + \\ \sum_{1 < j} \left[\frac{A_{ij}}{R_{ij}^{12}} - \frac{B_{ij}}{R_{ij}^{6}} + \frac{q_i q_j}{\varepsilon R_{ij}}\right], \end{split}$$

where r_{eq} and θ_{eq} are the equilibrium bond distance and equilibrium angle value, respectively, k_{bond} , k_{angle} , and $k_{dihedral}$ are force constants, and A, B, q and ε are parameters that characterize the non-bonded interactions.

The configuration files were pre-processed with AM1BCC, PARMCHECK and TLEAP codes that are part of the package [70], where AM1BCC determines the partial charges, PARMCHECK checks the forcefield if all parameters are defined in GAFF, and TLEAP prepares AMBER topology and coordinate files. The files created by TLEAP were then used to create individual LAMMPS data files by using the AMBER2LAMMPS Python script that ships with the LAMMPS package. To assemble everything into the systems, the coordinates of individual molecules were packed together using Packmol [71, 72] from the individual pdb files. An in-house code was used to integrate the forcefield parameters and the molecules/ions coordinates to build the LAMMPS data and input files. The simulation box was periodic in all directions. In system (i), it contained 45120 atoms with dimensions of $51.576\,\text{Å}\times$ $59.55484 \text{ Å} \times 360 \text{ Å}$ (Volume (V) = 1105776.15 Å^3). In system (ii), it contained 69500 of $91.0847 \text{ Å} \times 91.0847 \text{ Å} \times 91.0847 \text{ Å} (V =$ dimensions atoms with average $755677.16 \, \text{Å}^3$). Also, in system (i), canonical NVT ensemble simulations were performed using LAMMPS, whereas in system (ii), the isobaric-isothermal NPT ensemble was used. Temperature and pressure were controlled by using a Nose-Hoover thermostat and barostat with damping parameters of 0.1 ps and 1 ps, respectively. Long-range electrostatic interactions were evaluated via the FFT-based particle-particle/particle-mesh (PPPM) method [73] with an accuracy of 10⁻⁴ and a cut-off for the Van der Waals potential was set to 1 nm. The equationsof-motion were integrated by using the velocity-Verlet scheme in LAMMPS with a timestep of 1 fs. The production runs of the simulations proceeded for up to 15 ns for systems (i) and (ii).

Trajectories were recorded every 5 ps at each temperature condition. The calculation of tail correction of the polymer/polymer interaction for non-homogeneous systems was not considered in this study (see the Supplementary data).

From the simulation trajectory data, we computed the intermediate incoherent scattering function I(q,t), which is the spatial Fourier transform of the self-part of the Van Hove correlation function. The I(q,t) was computed for free and bound chains over a q-range of 1 nm⁻¹ to 15 nm⁻¹ for both temperature conditions using eq. (2).

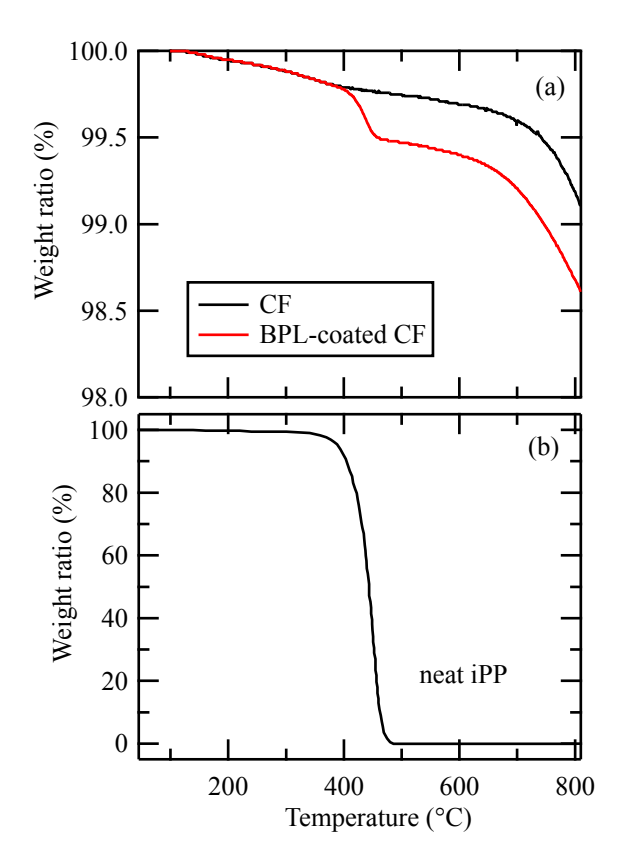


Fig. 2. (a) TGA results for the BPL-coated CF and bare CF and (b) the neat iPP.

3. Result and Discussion

3.1 Thermal properties of the BPL

Fig. 2a shows the TGA curves of the BPL-coated CF and bare CF samples. With respect to the iPP bulk data shown in Fig. 2b, the reduction of weight at around 400 °C corresponds to the weight loss of the BPL, while the second degradation temperature at around 650 °C is due to the weight loss of CF. To estimate the thickness of the BPL on the CF surface, two assumptions were made: (i) a core (i.e., CF)-shell (i.e., BPL) cylinder geometry, and (ii) that the density of the BPL remains the same as the bulk. The weight fraction of the BPL relative to the BPL-coated CF was estimated to be 0.5 %, giving us the BPL thickness of about 7 nm.

Fig. 3a shows the DSC results for the BPL-coated CF and bare CF. As expanded by the DSC data near the bulk melting temperature of iPP ($T_{\rm m} = 164$ °C determined by DSC), the endothermic peak during a heating process for the BPL-coated CF is identified at 164°C (Fig. 3b). This indicates the presence of a crystalline structure in the BPL. Moreover, the $T_{\rm m}$ value

of the BPL is the same as its correspondent for the neat iPP. Based on the total endothermic heat along with the heat fusion of a 100% iPP crystal sample ($\Delta H = 207$ J/g [74]), we estimated the degree of crystallinity of the BPL to be 19%, which is much smaller than that of the bulk (46% [75]). As will be discussed later, the backbone and side groups of the BPL lie nearly flat on the CF surface to increase the number of segment-solid contacts. Hence, we anticipate that the chain mobility is significantly reduced, rendering the crystallization of bound chains difficult even when the temperature is below the melting temperature.

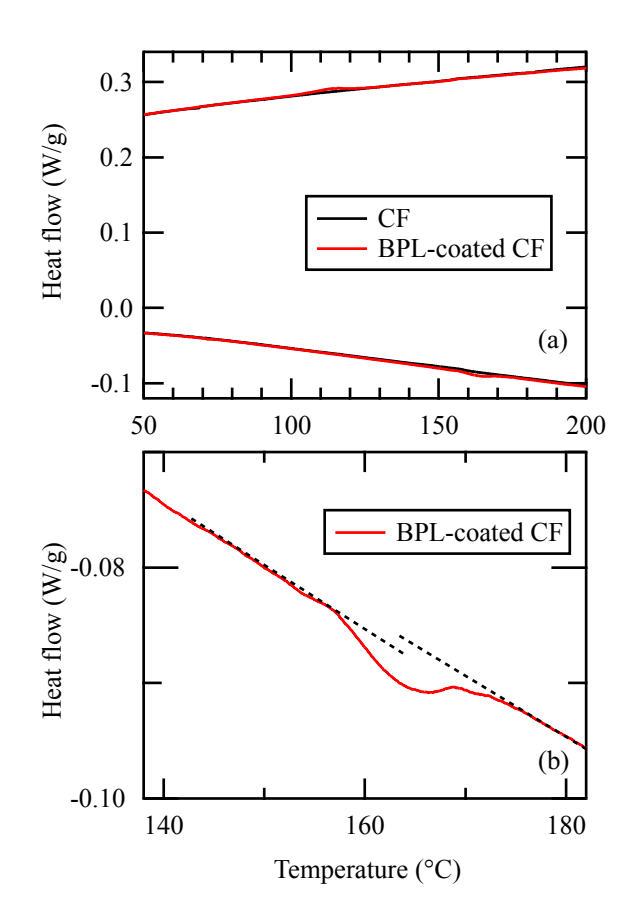


Fig. 3. (a) DSC curves of the BPL coated CF and bare CF. (b) Expanded view of the DSC curve of the BPL-coated CF near the bulk melting temperature.

3.2 Structure of BPL - SANS results

Fig. 4 shows the corrected SANS profile for the BPL-coated CF in d-xylene subtracted by the scattering from d-xylene and CF at 20 °C. From the data, we can see a broad scattering peak at q = 0.4 nm⁻¹. To further quantify the data, a core-shell-cylinder model [63] was used to discuss the structural information about the BPL. Since the size and length of the CF is far beyond the resolution of the SANS instrument, the effects of their sizes and polydispersity on the fitting results are minimal. The best-fit to the data gave us the BPL thickness of 5.0 ± 0.8 nm. The SLD of the BPL was estimated to be -3.2×10^{-5} nm⁻², which is identical to that of the bulk. The result indicates that there is no penetration of the solvent into the BPL at 20 °C, indicating that the crystalline structures formed in the BPL in d-xylene at 20 °C remain unchanged [61] and that the solvent acts like a poor solvent. Given the results, the thickness of the BPL in d-xylene can be considered as that in air. The thickness is in good agreement with

that estimated from the TGA result, suggesting that the BPL covers the CF surface entirely.

3.3 Structures of BPL - MD Simulations

Fig. 5 shows the monomer density distribution of the BPL along the z-direction calculated from the MD results for system (i). This distribution was extracted for both temperature conditions to mimic the QENS experiments. The thickness of the BPL was about 5.5 nm, which is in good agreement

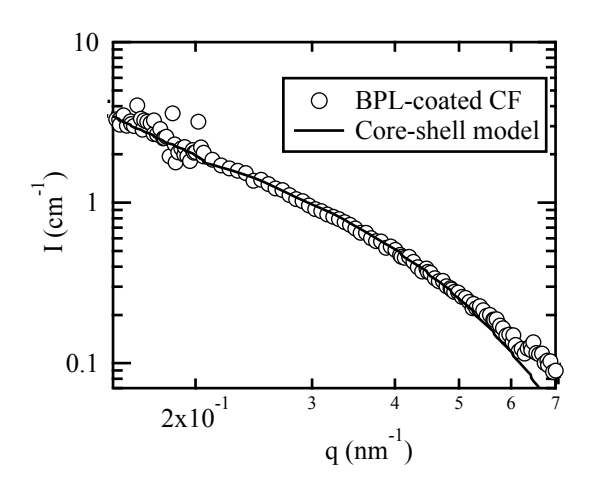


Fig. 4. SANS profile for the BPL-coated CF (circles) at 20 °C and best-fit result (solid line) based on a core-shell model. The diameter of CF was estimated to be around 6.8 μ m from SEM image analysis.

with the SANS results. As reported previously [33, 48], there is a high-density region (\sim 1 nm in thickness) near the filler surface. This agrees with several simulation results in the literature that investigated the effect of polymer/substrate interaction on the dynamics of polymer chains near the substrate [57, 76-80]. We also observed a weak temperature dependence of the monomer density profile. The average density of the BPL decreased from 0.730 ± 0.01 g/ml to 0.712 ± 0.01 g/ml g/ml at 183 °C and 220 °C, respectively, while the thickness increases from

5.50 nm to 5.65 nm. Hence, the total mass was conserved. The simulated density values are within 3% of the experimental values of iPP ($\cong 0.75~g/ml$ at 183 °C and $\cong 0.73~g/ml$ 220 °C, respectively) and the temperature dependence of the simulated density is in good agreement with the literature [81]. The volume fraction of the high-density region (at $z \leq 2.1~nm$) remained unchanged (~ 0.1).

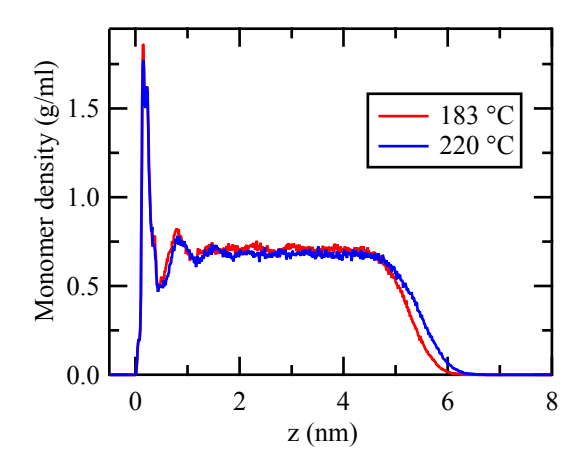


Fig. 5. Simulated monomer density distributions of the BPL along the z-direction at 183 °C and 220 °C. z=0 corresponds to the CF surface.

3.4 Segmental Dynamics of iPP bound layer – QENS

Fig. 6 shows the representative dynamic structure factor S(q,E) for (a) the bulk iPP (hereafter denoted by "free chains") and (b) the BPL-coated CF (hereafter denoted by "bound chains") at q = 6.25 nm⁻¹ and T = 183 °C. We first fit the $S(q,\omega)$ for the free chains with the Kohlrausch-Williams-Watts (KWW) equation (i.e., an intermediate scattering function $S(q,t) \propto \exp\left[-(t/\tau_B(q))^{\gamma}\right]$ [82, 83]) by applying the energy Fourier Transformation of $S(q,\omega)$ to fit in the energy domain,

$$S(q, \omega) = \left(A_{KWW} \mathfrak{F}\left[\exp\left[-\left(\frac{t}{\tau_B(q)}\right)^{\gamma}\right]\right]\right) \otimes R(q, \omega), (4)$$

where $A_{\rm KWW}$ is a numerical constant, $\tau_B(q)$ is the segmental relaxation time, and γ is the stretching exponent. \mathfrak{F} denotes the Fourier transformation, $R(q,\omega)$ is the resolution function, and \otimes represents a convolution operator. It has been reported that $\gamma \cong 0.5$ is established for many polymers [83]. The exponent of $\gamma = 0.5$ for the segmental dynamics in polymer melts is predicted by the standard Rouse model [84]. As shown in Fig. 6a, we confirmed that $\gamma = 0.5$ reasonably satisfied the fitting results for the free chains regardless of q within the q-range. Hence, we used the fixed value of $\gamma = 0.5$ for all the fitting procedures. Also, the reasonable fit of the experimental data with eq. (4) implies that the contribution of the fast vibration (on the order of 0.5 ps [85]) for iPP melts, which will be discussed in the next section, can be ignored.

For the BPL chains (shown in Fig. 6b), both elastic and quasi elastic scattering were detected. There are two contributions in the elastic component: one originates from the internal inhomogeneous (the so-called turbostratic) structures within CF [86] whose size is less than 1 nm [87] and the other originates from "immobile" segments strongly adsorbed on the CF surface [88]. Fig. 6c shows the $S(q,\omega)$ of the BPL-coated CF and bare CF, where the $S(q,\omega)$ of the bare CF was normalized by the ratio of the weight of CF and the BPL-coated CF. The $S(q,\omega)$ of the BPL-coated CF is higher than that of CF, indicating the presence of "immobile" components within the BPL. To evaluate the spectra from the BPL-coated CF, we approximated $S(q,\omega)$ as the sum of the KWW function and elastic contribution, *i.e.*,

$$S(q,\omega) = \left(A_B \mathfrak{F}\left[\exp\left[-\left(\frac{t}{\tau_B(q)}\right)^{\gamma}\right]\right] + A_d \delta(\omega)\right) \otimes R(q,\omega), (5)$$

where $A_{\rm B}$ and $A_{\rm d}$ ($A_{\rm B}+A_{\rm d}=1$) are numerical constants and $\delta(\omega)$ is a delta function that is approximated to express the elastic contribution. Representative fitting results at 183°C are shown in Fig. 6b, demonstrating that eq.

(5) is appropriate regardless of q. Since it is experimentally difficult to separate the two contributions of the elastic scattering, we will quantify the immobile fraction of bound chains based on the MD results.

Fig. 7 summarizes the q dependence of $\tau_B(q)$ for both the bound and the free iPP chains at (a) 183 °C and (b) 220°C. It has been reported that the power-law, $\tau_B^{\gamma}(q) \propto q^{-2}$, is established for many polymers in the limit of low q values ($q \le$ 10 nm⁻¹) [83], indicating that the dynamics is originated from the segmental dynamics described by the standard Rouse model [83, 84]. The data shows the powerlaw behavior of $\tau_B^{0.5}(q) \propto q^{-\alpha}$ ($\alpha =$ 1.55 ± 0.05) for the free chains at q < 9nm⁻¹. Hence, the power law exponent is slightly smaller than the Rouse model, but is consistent with previous QENS data for iPP melts at similar temperatures [89]. This discrepancy may be attributed to the contribution of methyl group rotations within the q and time domains of QENS measurements, as previously reported [89]. However, the separation of these

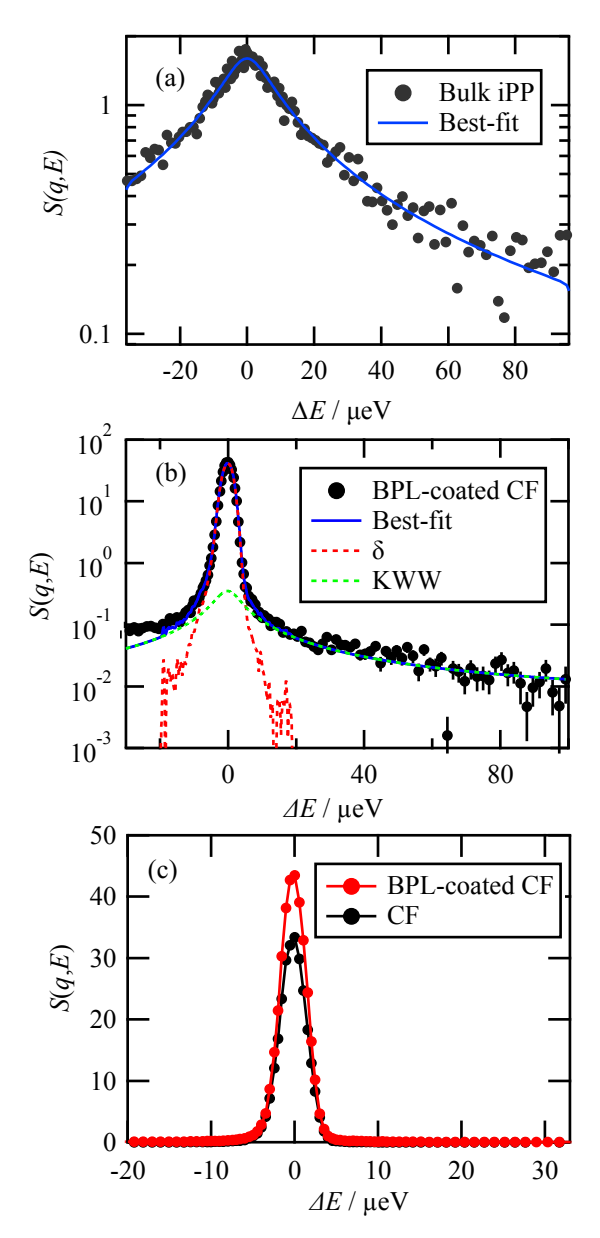


Fig. 6. Comparisons of QENS spectra for (a) the iPP, (b) the BPL-coated CF, and (c) the BPL-coated CF and bare CF at $q = 6.25 \text{ nm}^{-1}$ and 183 °C. The solid lines (indicated in blue) correspond to the best-fit of the KWW equation to the iPP sample. There are additional elastic contributions that result from immobile polymer segments in the BPL-coated CF (shown by the red line in (c)) relative to the bare CF (shown by the black line in (c)).

contributions is difficult from an experimental point of view without selective isotope labeling. A deviation from the power-law indicates the non-Gaussian statistics of molecular displacements at small length scales [90-93]. Furthermore, the QENS data indicates that the dynamics of bound chains is much faster at the relatively low q region than those of free chains at both temperatures, while the deviation disappears at the higher q region.

We previously reported, using QENS, that the segmental dynamics of bound polybutadiene (PB) chains onto the CB surface in a PB melt is identical to that of free chains in the melt within the given qrange $(4 < q < 18 \text{ nm}^{-1})$ [48]. On the other hand, QENS results reported by Roh and co-workers showed the suppressed segmental dynamics of exposed PB bound chains on the CB surface (without a matrix) compared to that of counterpart free chains [93]. However, their conclusion was derived from $S(q, \omega)$ summed over all qvalues $(3.1 < q < 17.1 \text{ nm}^{-1})$ used for the QENS measurements. To further shed light into the interfacial dynamics, in the following section, we aim at clarifying the dynamics of free and bound chains that

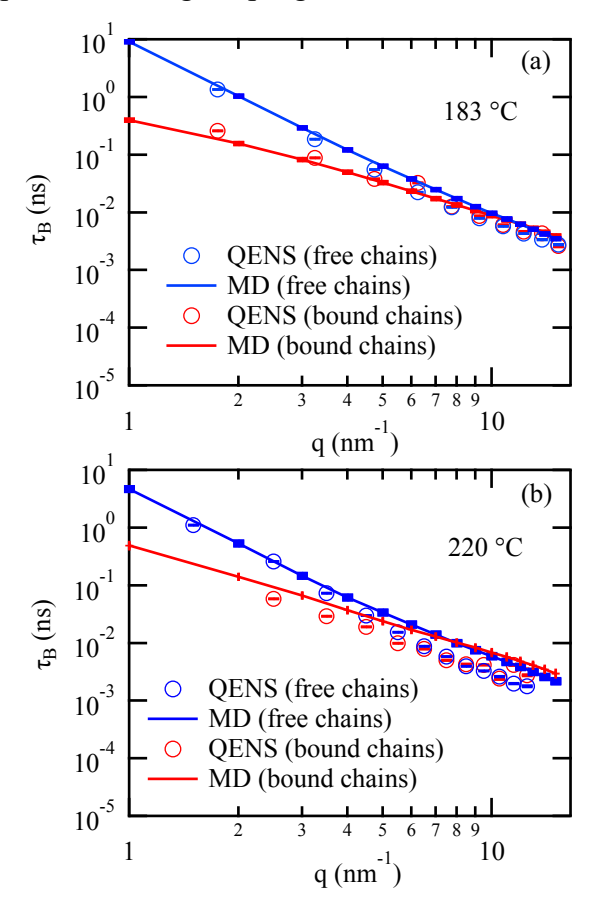


Fig. 7. Comparison of segmental dynamics of bound and free iPP chains (a) at 183 °C and (b) at 220 °C. The symbols and solid lines correspond to the QENS data and MD data, respectively.

span the time domain from sub-ps to 15 ns using atomistic MD simulations.

3.5 Segmental and Local Dynamics of Bound Chains – **MD simulations.** Fig. 8 shows representative computed I(q,t) data for (a) free and (b) bound chains at 183 °C using eq. (4). Tanchawanich and co-workers [89] demonstrated the product of two independent contributions to describe the intermediate scattering function for iPP melts at $T > T_{\rm m}$:

$$I(q,t) = I^{lib}(q,t)I^{seg}(q,t), (6)$$

where $I^{lib}(q,t)$ represents the fast vibration on the picosecond time scale which is identified with oscillations around energy minima, and $I^{seg}(q,t)$ accounts for the slow segmental motion [89]. As mentioned above, $\tau_B(q)$ determined from the QENS data may include the contribution of methyl group rotations. We therefore used eq. (6) and compared the "effective" characteristic time of the slow mode, $\langle \tau_B \rangle$, extracted from the computed I(q,t) with those determined from the QENS data. Taking further input from the prior study [89], we used an exponential decay function to describe the fast dynamics, as well as a KWW stretch exponential function to describe the slow mode:

$$I^{bulk}(q,t) = \left[A_f(q) + (1 - A_f(q)) \exp\left(-\frac{t}{\tau_{fast}}\right) \right] \exp\left(-\frac{t}{\langle \tau_B \rangle}\right)^{\gamma}, (7)$$

with τ_{fast} being the characteristic time of the localized relaxations, the order of 0.5 ps for iPP [85], and $A_f(q)$ being the temperature-dependent amplitude of the fast process. As performed for the QENS analysis, we further expanded this function to describe the motions of bound chains on the CF surfaces as follows:

$$I^{bound}(q, t) = [I^{bulk}(q, t)A_m + (1 - A_m)], (8)$$

where A_m is treated as the volume fraction of a mobile component, and $(1 - A_m)$ the immobile counterpart. The presence of the immobile component is evidenced as a plateau at long times in Fig. 8b. The best-fits to the data with eq. (8) gave us the constant immobile fraction of 0.02-0.03 at q > 5 nm⁻¹ for both temperature conditions. As discussed above, the volume fraction of the high-density region at z < 1.0 nm is about 0.1 (Fig. 5). Hence, these results suggest that while the trains are densely packed and give rise to the higher density, most of the H atoms located in the trains (i.e., adsorbed parts) still vibrate within the MD time scale.

Fig. 7 also plots $\langle \tau_B \rangle$ extracted from the computed I(q,t). Hence, the MD simulations predict the overall experimental results probed by QENS in a satisfactory manner except for the high q data at 220 °C. Since the measured energy transfer range is limited ($\Delta E_{max} = 100 \, \mu eV$) compared to the broadening of QENS at 220 °C, we expect that the experimental τ_B values from QENS are underestimated. Nevertheless, it is reasonable to conclude that the enhanced slow mode at the relatively low q region is inherent to the bound chains. This result

may be consistent with previous MD results on a polystyrene bound layer on a planar substrate that indicated the presence of a "free surface" region at the topmost surface of the bound layer (about 2 nm in thickness) where the segmental dynamics is enhanced compared to the bulk regardless of polymer-substrate interactions [80].

Note that the τ_{fast} estimated from the best fits to the data with eq. (6) varied from 0.5 ps to 2.5 ps with different q. Prior experimental and computational studies reported to be $\tau_{fast} \approx 0.5$ ps, independent of q [89, 94]. In addition, the γ values deviated from 0.5 for both bound ($\gamma = 0.67$ -0.98) and free ($\gamma = 0.6$ -0.75) chains. These discrepancies suggests the contribution of methyl group rotations to the computed I(q,t).

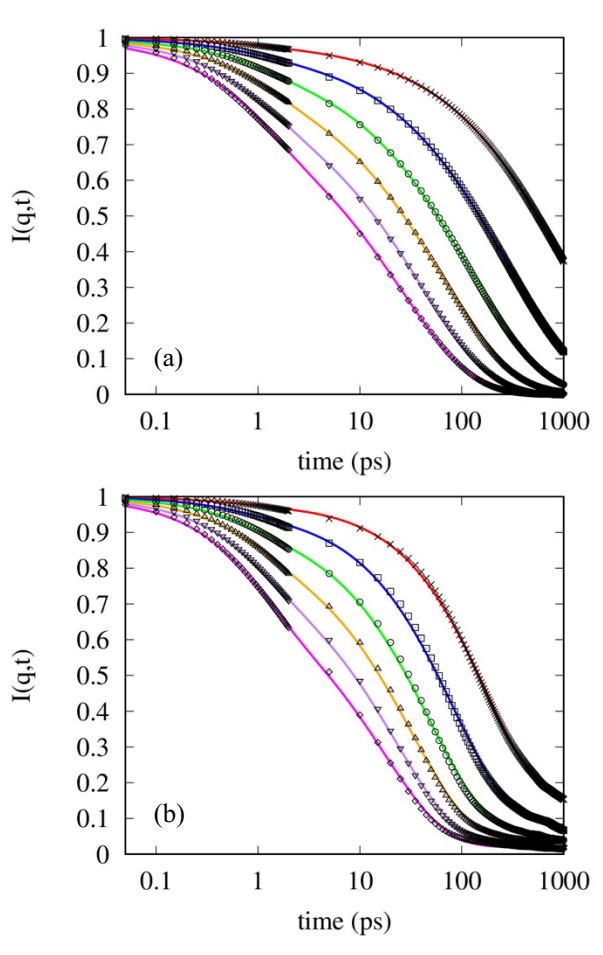


Fig. 8. Representative computed I(q,t) data for (a) free and (b) bound chains at 183 °C in the q-range of 2 nm⁻¹ to 7 nm⁻¹. The q-values increase from the topmost to bottommost curve, respectively.

We are currently working on "selective labeling" where the same I(q,t) computation methodology is applied, except that only side-group respective H atom trajectories will be considered to discuss the dynamics of the side groups independently. The details will be summarized in a forthcoming publication.

Finally, we discuss the orientations of backbone chains and side groups composed of bound chains on the CF surface to gain insight into the chain conformations. From the LAMMPS trajectory files for production runs used to compute I(q,t) in system (i), we used the atom coordinate data (i.e., x_u , y_u , and z_u) to initialize a positional bond vector equivalent to (a) the sum of all C-H bond vectors (v_s) in side group chains (CH₃) and (b) the sum of all C-C bond vectors (v_b) in backbone chains (see, Fig. 9a). Using the z-axis in LAMMPS as a directional reference point, we took the dot product of the three resultant (x_u , y_u , z_u) vectors to find θ_t

between each of the vectors and the z-axis. The second Legendre polynomial distribution of θ_t , $P_2(z) = 1.5\langle\cos^2\theta_t\rangle - 0.5$, was then calculated as a function of z so that a coefficient could be used to indicate the orientations, as well a number density distribution of C atoms involved in the calculation. We used a 0.01 nm-thick slab to calculate $P_2(z)$ for the bound chains in the z-direction (i.e., the direction perpendicular to the CF surface).

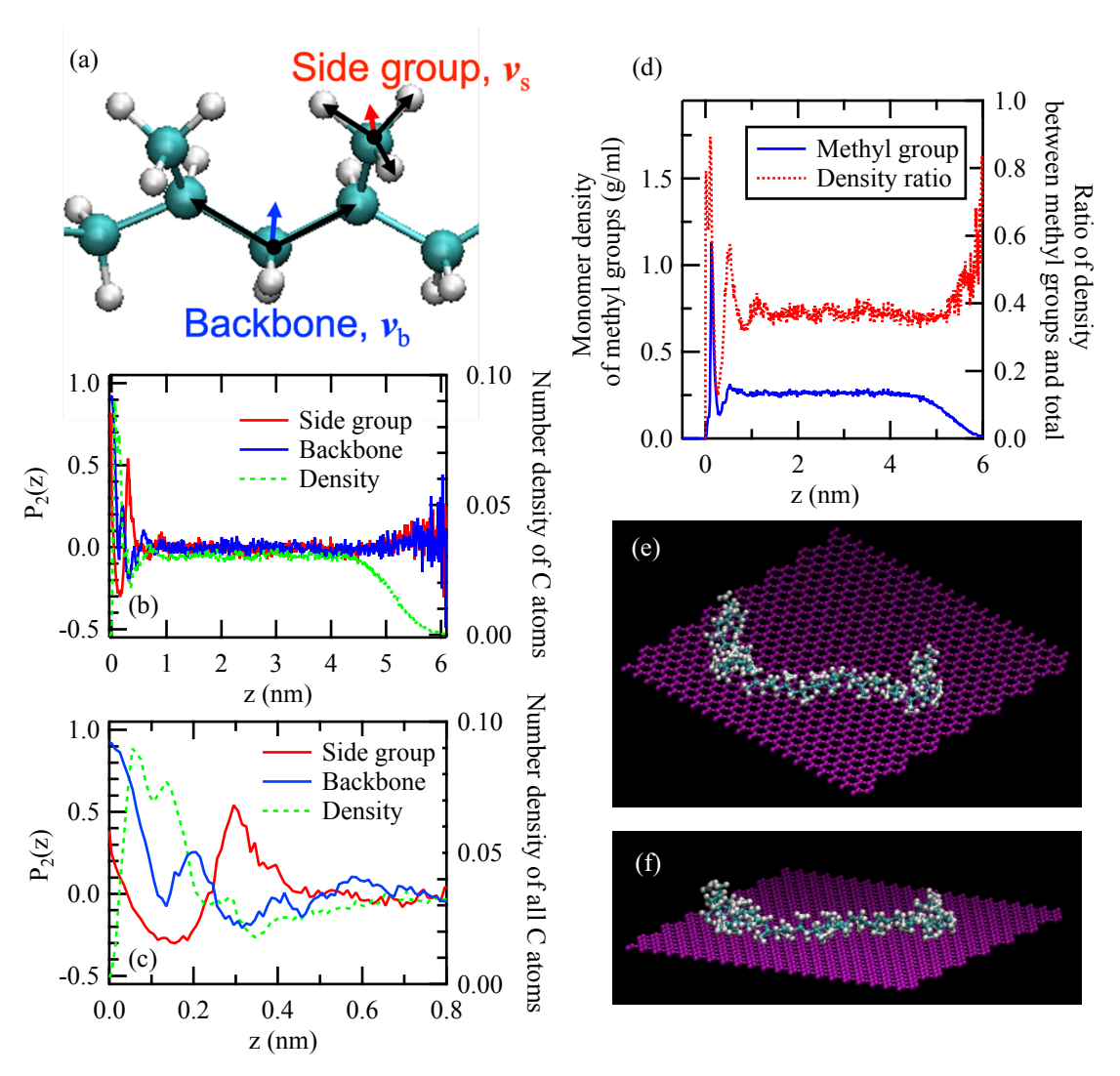


Fig. 9. (a) Schematic illustration of iPP chains and the definitions of the respective bond vectors to calculate P_2 . C and H atoms are indicated by green and white colors, respectively. (b) P_2 values as a function of z for summed C-H bond vectors in the side groups and C-C bond vectors in the backbone chains composed of bound chains at 183 °C. The number density distribution of all C atoms (both the backbone and side group) involved in the calculation is also plotted. (c) Expanded view of Figure (a) near the CF surface. The CF/polymer interface corresponds to z = 0. (d) Simulated monomer density distributions of the BPL methyl group compared with the ratio of the methyl group and total BPL monomer density distributions along the z-direction at 183 °C. Snapshot of iPP chains near the CF surface: (d) top and (e) side views. C and H atoms of an iPP chain are indicated by green and white colors, respectively. C atoms of CF are indicated by a purple color.

Fig. 9b shows $P_2(z)$ of the backbone and side groups of bound chains along with the number density of all carbon atoms binned in the z-direction at 183 °C. P₂ for both backbone and side groups remained nearly 0 at z > 0.8 nm, indicating that the backbone and side groups are randomly oriented. On the other hand, as highlighted in Fig. 9c, the P_2 values oscillate between -0.3 and 0.9 at z < 0.8 nm, suggesting that the backbone and side groups have rather dominant orientations against the CF surface. Note that the P_2 values of 1 and -0.5 correspond to $\theta_t = 0$ (a "flat" configuration, i.e., backbone/side groups are oriented in the direction parallel to the CF surface) and $\theta_t = 90^\circ$ (a "standing" configuration, i.e., backbone/side groups are oriented in the direction perpendicular to the CF surface), respectively. Hence, it is indicative that the backbone chains lie nearly flat on the CF surface. This is in consistent with previous atomistic MD results for atactic PP (aPP) chains (below the glass transition temperature (T_g)) on a graphite surface [54]. The same tendency of backbone orientations was indicative at the poly(methyl methacrylate) (PMMA)/graphene interface at $T > T_g$ regardless of the choice of tacticity [59]. To further provide insight into the orientation of the side groups, we calculated the monomer density distribution of the side group as a function of z at 183 °C. The calculation methodology to produce Fig. 9d considered only side-group respective C and H atom densities but was otherwise retained from Fig. 5. We found that the density of the side groups in the bound chains was significantly enhanced near the CF surface. This finding in conjunction with $P_2 > 0$ near the CF surface indicates that the side groups also prefer to lie flat on the CF surface. The result is in contrast to the aforementioned previous MD results for aPP chains on a graphite surface where the side groups showed a preferential perpendicular orientation with respect to the surface [54]. We expect that this is attributed to the difference in chain packing at the graphite interface between iPP and aPP. In fact, Behbahani and co-workers predicted that the chain packing of isotactic PMMA is better than that of syndiotactic PMMA or atactic PMMA on graphene [59].

Fig. 9d shows the ratio of the density between the side groups and the total (shown in Fig. 5). Hence, the side groups tend to migrate not only to the CF-vacuum interface but also the polymer-CF interface. The former is consistent with previous results [95, 96] and possibly due to the decreased steric hinderance between neighboring methyl groups. The latter indicates that

both the backbone and side group lie nearly flat on the CF surface (as highlighted in Fig. 9e and 9f) to increase the number of solid/backbone segment contacts, which is the driving force for the "flattening" process of bound chains to overcome the conformational entropy loss in the total free energy, as revealed for bound chains formed in supported polymer thin films [97-99]. The chain arrangements result in the improvement of segmental packing near the CF surface, as evidenced in Fig. 5. Using the selective labeling approach, the effects of tacticity on the flattening process of PP on solids with different segment-solid interactions are currently in progress. For the backbone and side chains of bound chains located slightly away from the CF surface (at z < 0.6 nm), they appear to show preferred orientations depending on z (Fig. 9c). & 9f). At z > 0.6 nm, however, their orientations become randomized (isotropic) (Fig. 9c).

4. Conclusion

In summary, we have studied the local conformations of bound iPP chains on the CF surface and the resultant dynamics at the relevant length and time scales at $T > T_{\rm m}$ using the integrated experimental-computational approaches. The results reveal novel local structural and dynamical features of bound iPP chains as well as the macroscopic properties: (i) the thickness of the bound layer is estimated to be about 5 nm; (ii) the formation of a high-density region (less than 1 nm in thickness) near the CF surface; (iii) the degree of crystallinity for the bound chains is quite lower than the bulk, while the melting temperature remains the same as the bulk, (iv) the presence of an immobile component in the bound layer whose fraction is only a few %, (v) the segmental dynamics of the bound chains at the relatively low q region is enhanced possibly due to the presence of a free surface region at the topmost surface of a bound layer, and (vi) the backbone and side groups of the bound chains lie flat on the CF surface, which would be unique to iPP chains and is the driving force for the flattening process to overcome the conformational entropy loss in the total free energy.

It is also interesting to note on the gradient in the segmental dynamics within the bound layer along the direction normal to the CF surface. This suggests the reduction of the glass transition temperature at the topmost surface [100]. At the same time, the presence of the free surface implies that the polymer-solid interaction is not strong such that the propagation of

suppressed dynamics induced by interacting substrates is limited [101] and/or preceded by the

lack of large loops (sequences of free segments connecting successive trains), which play

crucial roles in propagating the suppressed interfacial dynamics into the film interior [102].

Further computational studies to quantify the detailed chain statistics about tails, loops, and

tails [97] deserve future work.

Author Information

Corresponding Authors

Email: tadanori.koga@stonybrook.edu (T. K.)

Email: maya.koga@stonybrook.edu (M. E.)

Author Contributions

The manuscript was written through contributions of all authors. All authors have given

approval to the final version of the manuscript.

Notes

The authors declare no competing financial interest.

Acknowledgments

T. K. and M. E. acknowledge financial support from Mitsui Chemicals Inc. T.K. also

acknowledges partial financial supports from National Science Foundation (DMR Polymers

2210207). Acknowledgment is also made to the Donors of the American Chemical Society

Petroleum Research Fund (ACS-PRF 59064-ND7) for partial support of this research. The

computational aspects of this work were performed at the Center for Nanophase Materials

Sciences (CNMS), a U.S. Department of Energy Office of Science User Facility at Oak Ridge

National Laboratory. This research also used resources of the Oak Ridge Leadership

Computing Facility (OLCF), which is a DOE Office of Science User Facility supported under

Contract DE-AC05-00OR22725. The QENS experiments at the Materials and Life Science

22

Experimental Facility of the J-PARC was performed under a user program (Proposal No. 2019B0178 and 2020C0004). The SANS experiments at the QUOKKA beamline of ANSTO was performed under a user program (Proposal No. 7557). The authors acknowledge Kathleen Wood, Jitendra Mata, and Anna Paradowska (ANSTO) for their assistance with the SANS experiments. The authors acknowledge the support of the Functional Polymer Consortium (FPC) and the Quantum Beam Analyses Alliance (QBAA).

References

- [1] S.K. Kumar, B.C. Benicewicz, R.A. Vaia, K.I. Winey, 50th Anniversary Perspective: Are Polymer Nanocomposites Practical for Applications?, Macromolecules 50 (2017) 714-731.
- [2] E.J. Bailey, K.I. Winey, Dynamics of polymer segments, polymer chains, and nanoparticles in polymer nanocomposite melts: A review, Prog. Polym. Sci. 105 (2020) 101242.
- [3] F.S. Wang, Y.Y. Ji, X.S. Yu, H. Chen, Z.F. Yue, Ablation damage assessment of aircraft carbon fiber/epoxy composite and its protection structures suffered from lightning strike, Compos Struct 145 (2016) 226-241.
- [4] A. Danish, M.A. Mosaberpanah, M.U. Salim, M. Amran, R. Fediuk, T. Ozbakkaloglu, M.F. Rashid, Utilization of recycled carbon fiber reinforced polymer in cementitious composites: A critical review, J. Build. Eng. 53 (2022) 104583.
- [5] J.H. Lu, J.P. Youngblood, Adhesive bonding of carbon fiber reinforced composite using UV-curing epoxy resin, Compos B. Eng. 82 (2015) 221-225.
- [6] T. Yamamoto, K. Uematsu, T. Irisawa, Y. Tanabe, Controlling of the interfacial shear strength between thermoplastic resin and carbon fiber by adsorbing polymer particles on carbon fiber using electrophoresis, Compos. Part A. Appl. Sci. 88 (2016) 75-78.
- [7] D. Hwang, D. Cho, Fiber aspect ratio effect on mechanical and thermal properties of carbon fiber/ABS composites via extrusion and long fiber thermoplastic processes, J. Ind. Eng. Chem. 80 (2019) 335-344.
- [8] S.S. Yao, F.L. Jin, K.Y. Rhee, D. Hui, S.J. Park, Recent advances in carbon-fiber-reinforced thermoplastic composites: A review, Compos B. Eng. 142 (2018) 241-250.
- [9] P. Szymoniak, B.R. Pauw, X. Qu, A. Schonhals, Competition of nanoparticle-induced

- mobilization and immobilization effects on segmental dynamics of an epoxy-based nanocomposite, Soft Matter 16(23) (2020) 5406-5421.
- [10] T. Yamamoto, S. Yabushita, T. Irisawa, Y. Tanabe, Enhancement of bending strength, thermal stability and recyclability of carbon-fiber-reinforced thermoplastics by using silica colloids, Compos. Sci. Technol. 181 (2019) 107665.
- [11] D.S. Villars, Studies on carbon black. III. Theory of bound rubber, J. Polym. Sci. 21 (1956) 257-271.
- [12] A.I. Medalia, Morphology of aggregates 6. Effective volume of aggregates of carbon black from electron microscopy. Application to vehicle absorption and to die swell of filled rubber, J. Colloid Interface Sci. 32 (1970) 115-131.
- [13] C.M. Blow, Polymer-particulate filler interaction- bound rubber phenomena, Polymer 14 (1973) 309-323.
- [14] E.M. Dannenberg, Bound rubber and carbon black reinforcement, Rubber Chem. Technol. 59 (1986) 512-524.
- [15] J.C. Kenny, V.J. McBrietry, Z. Rigbi, D.C. Douglass, Carbon black filled natural rubber 1. Structural investigations, Macromolecules 24 (1991) 436-443.
- [16] L. Karasek, M. Sumita, Characterization of dispersion state of filler and polymer-filler interactions in rubber carbon black composites, J. Mater. Sci. 31 (1996) 281-289.
- [17] S.I. Ono, M.; Tokumitsu, H.; Seki, K., Structure Development in Silica-Filled PolyacrylateRubber Composites During Mixing, J. Appl. Polym. Sci. 74 (1999) 2529-2538.
- [18] J.W.t. Brinke, V.M. Litvinov, J.E.G.J. Wijnhoven, J.W.M. Noordermeer, Interactions of Sto"ber Silica with Natural Rubber under the Influence of Coupling Agents, Studied by 1H NMR T2 Relaxation Analysis, Macromolecules 35 (2002) 10026-10037.
- [19] S.E. Harton, S.K. Kumar, H.C. Yang, T. Koga, K. Hicks, E. Lee, J. Mijovic, M. Liu, R.S. Vallery, D.W. Gidley, Immobilized Polymer Layers on Spherical Nanoparticles, Macromolecules 43 (2010) 3415-3421.
- [20] N. Jouault, J.F. Moll, D. Meng, K. Windsor, S. Ramcharan, C. Kearney, S.K. Kumar, Bound Polymer Layer in Nanocomposites, ACS Macro Lett. 2 (2013) 371-374.
- [21] N. Jiang, M.K. Endoh, T. Koga, T. Masui, H. Kishimoto, M. Nagao, S.K. Satija, T.

- Taniguchi, Nanostructures and Dynamics of Macromolecules Bound to Attractive Filler Surfaces, ACS Macro Lett. 4 (2015) 838-842.
- [22] G.P. Baeza, C. Dessi, S. Costanzo, D. Zhao, S. Gong, A. Alegria, R.H. Colby, M. Rubinstein, D. Vlassopoulos, S.K. Kumar, Network dynamics in nanofilled polymers, Nat. Commun. 7 (2016) 11368.
- [23] P.J. Griffin, V. Bocharova, L.R. Middleton, R.J. Composto, N. Clarke, K.S. Schweizer, K.I. Winey, Influence of the Bound Polymer Layer on Nanoparticle Diffusion in Polymer Melts, ACS Macro Lett. 5 (2016) 1141-1145.
- [24] N. Jouault, M.K. Crawford, C. Chi, R.J. Smalley, B. Wood, J. Jestin, Y.B. Melnichenko, L. He, W.E. Guise, S.K. Kumar, Polymer Chain Behavior in Polymer Nanocomposites with Attractive Interactions, ACS Macro Lett. 5 (2016) 523–527.
- [25] T. Koga, D. Barkley, M. Nagao, T. Taniguchi, J.-M.Y. Carrillo, B.G. Sumpter, T. Masui, H. Kishimoto, M. Koga, J.G. Rudick, M.K. Endoh, Interphase structures and dynamics near nanofiller surfaces in polymer solutions, Macromolecules 51 (2018) 9462-9470.
- [26] A.M. Jimenez, D. Zhao, K. Misquitta, J. Jestin, S.K. Kumar, Exchange Lifetimes of the Bound Polymer Layer on Silica Nanoparticles, ACS Macro Lett. 8 (2019) 166-171.
- [27] I. Popov, B. Carroll, V. Bocharova, A.-C. Genix, S. Cheng, A. Khamzin, A. Kisliuk, A.P. Sokolov, Strong Reduction in Amplitude of the Interfacial Segmental Dynamics in Polymer Nanocomposites, Macromolecules 53 (2020) 4126-4135.
- [28] R. Simha, H.L. Frisch, F.R. Eirich, The Adsorption of Flexible Macromolecules, J. Phys. Chem. 57 (1953) 584-589.
- [29] S. Merabia, P. Sotta, D.R. Long, A microscopic model for the reinforcement and the nonlinear behavior of filled elastomers and themoplastic elastomers (Payne and Mullins effects), Macromolecules 41 (2008) 8252-8266.
- [30] M. Qu, F. Deng, S.M. Kalkhoran, A. Gouldstone, A. Robisson, K.J.V. Vliet, Nanoscale visualization and multiscale mechanical implications of bound rubber interphases in rubber–carbon black nanocomposites, Soft Matter 7 (2011) 1066–1077.
- [31] K. Nakajima, T. NIshi, Recent Development in Rubber Research using Atomic Force Microscopy, in: A.K. Bhomik (Ed.), Current Topics in Elastomer Research, CRC Press, FL,

- 1008, pp. 579-604.
- [32] A. Papon, H. Montes, M. Hanafi, F. Lequeux, L. Guy, K. Saalwachter, Glass-Transition Temperature Gradient in Nanocomposites: Evidence from Nuclear Magnetic Resonance and Differential Scanning Calorimetry, Phys. Rev. Lett. 108 (2012) 065702.
- [33] H. Mortazavian, C.J. Fennell, F.D. Blum, Structure of the Interfacial Region in Adsorbed Poly(vinyl acetate) on Silica, Macromolecules 49 (2016) 298-307.
- [34] J. Yang, M. Melton, R. Sun, W. Yang, S. Cheng, Decoupling the Polymer Dynamics and the Nanoparticle Network Dynamics of Polymer Nanocomposites through Dielectric Spectroscopy and Rheology, Macromolecules 53 (2020) 302-311.
- [35] Y. Zhou, B. Yavitt, Z. Zhou, V. Bocharova, D. Salatto, M. Endoh, A. Ribbe, A. Sokolov, T. Koga, K.S. Schweizer, Bridging Controlled Network Microstructure and Long Wavelength Fluctuations in Silica-Poly(2-vinylpyridine) Nanocomposites: Experimental Results and Theoretical Analysis, Macromolecules 53 (2020) 6984–6994.
- [36] B.M. Yavitt, D. Salatto, Y. Zhou, Z. Huang, M.K. Endoh, L. Wiegart, V. Bocharova, A.E. Ribbe, A.P. Sokolov, K.S. Schweizer, T. Koga, Collective Nanoparticle Dynamics Associated with Bridging Network Formation in Model Polymer Nanocomposites, ACS Nano 15 (2021) 11501-11513.
- [37] S. Merabia, P. Sotta, D.R. Long, Unique plastic and recovery behavior of nanofiled elastomers and thermoplastic elastomers (Payne and Mullins effects), J. Polym. Sci., Part B, Polym. Phys. 48 (2010) 1495-1508.
- [38] Q. Chen, S. Gong, J. Moll, D. Zhao, S.K. Kumar, R.H. Colby, Mechanical Reinforcement of Polymer Nanocomposites from Percolation of a Nanoparticle Network, ACS Macro Lett. 4 (2015) 398-402.
- [39] D. Zhao, S. Ge, E. Senses, P. Akcora, J. Jestin, S.K. Kumar, Role of Filler Shape and Connectivity on the Viscoelastic Behavior in Polymer Nanocomposites, Macromolecules 48 (2015) 5433-5438.
- [40] A. Mujtaba, M. Keller, S. Ilisch, H.-J. Radusch, T. Thurn-Albrecht, K. Saalwachter, M. Beiner, Mechanical properties and cross-link density of styrene-butadiene model composites containing fillers with bimodal particle size distribution, Macromolecules 45 (2012) 6504-6515.

- [41] A. Mujtaba, M. Keller, S. Ilisch, H.-J. Radusch, M. Beiner, T. Thurn-Albrecht, K. Saalwachter, Detection of surface-immoblized components and their role in viscoelastic reinforcement of rubber-silica nanocomposites, ACS Macro Lett. 3 (2014) 481-485.
- [42] Y. Zhou, B.M. Yavitt, Z. Zhou, V. Bocharova, D. Salatto, M.K. Endoh, A.E. Ribbe, A.P. Sokolov, T. Koga, K.S. Schweizer, Bridging Controlled Network Microstructure and Long Wavelength Fluctuations in Silica-Poly(2-vinylpyridine) Nanocomposites: Experimental Results and Theoretical Analysis, Macromolecules 53 (2020) 6984-6994.
- [43] A. Mujtaba, M. Keller, S. Ilisch, H.J. Radusch, M. Beiner, T. Thurn-Albrecht, K. Saalwachter, Detection of Surface-Immobilized Components and Their Role in Viscoelastic Reinforcement of Rubber-Silica Nanocomposites, ACS Macro Lett. 3 (2014) 481-485.
- [44] A. Papon, S. Merabia, L. Guy, F. Lequeux, H. Montes, P. Sotta, D.R. Long, Unique Nonlinear Behavior of Nano-Filled Elastomers: From the Onset of Strain Softening to Large Amplitude Shear Deformations, Macromolecules 45 (2012) 2891–2904.
- [45] A.R. Payne, The dynamic properties of carbon black-loaded natural rubber vulcanizates. Part I, J. Appl. Polym. Sci. 6 (1962) 57-63.
- [46] A.R. Payne, A note on the conductivity and modulus of carbon black-loaded rubbers, J. Appl. Polym. Sci. 9 (1965) 1073-1082.
- [47] M. Divandari, G. Morgese, L. Trachsel, M. Romio, E.S. Dehghani, J.-G. Rosenboom, C. Paradisi, M. Zenobi-Wong, S.N. Ramakrishna, E.M. Benetti, Topology Effects on the Structural and Physicochemical Properties of Polymer Brushes, Macromolecules 50 (2017) 7760-7769.
- [48] D. Salatto, J.-M.Y. Carrillo, M.K. Endoh, T. Taniguchi, B.M. Yavitt, T. Masui, H. Kishimoto, M. Tyagi, A.E. Ribbe, V.G. Sakai, M. Kruteva, B.G. Sumpter, B. Farago, D. Richter, M. Nagao, T. Koga, Structural and dynamical roles of bound polymer chains in rubber reinforcement, Macromolecules 54 (2021) 11032-11046.
- [49] E. Senses, A. Faraone, P. Akcora, Microscopic Chain Motion in Polymer Nanocomposites with Dynamically Asymmetric Interphases, Sci. Rep. 6 (2016) 29326.
- [50] W. Cui, W. You, W. Yu, Mechanism of Mechanical Reinforcement for Weakly Attractive Nanocomposites in Glassy and Rubbery States, Macromolecules 54 (2021) 824-834.

- [51] E. Raphael, P.G.D. Gennes, Rubber-rubber adhesion with connector molecules, J. Phys. Chem. 96 (1992) 4002–4007.
- [52] S. Rose, A. Prevoteau, P. Elzière, D. Hourdet, A. Marcellan, L. Leibler, Nanoparticle solutions as adhesives for gels and biological tissues, Nature 505 (2014) 382-385.
- [53] A.C. Genix, V. Bocharova, A. Kisliuk, B. Carrol, S. Zhao, J. Oberdisse, A.P. Sokolov, Enhancing the mechanical properties of glassy nanocomposites by tuning polymer molecular weight, ACS Appl. Mater. Interfaces 10 (2018) 33601-33610.
- [54] K.F. Mansfield, D.N. Theodorou, Molecular Dynamics Simulation of a Glassy Polymer Surface, Macromolecules 24 (1991) 6283-6294.
- [55] V.A. Harmandaris, K.C. Daoulas, V.G. Mavrantzas, Molecular Dynamics Simulation of a Polymer Melt/Solid Interface: Local Dynamics and Chain Mobility in a Thin Film of Polyethylene Melt Adsorbed on Graphite, Macromolecules 38 (2005) 5796-5809.
- [56] A.N. Rissanou, V. Harmandaris, Dynamics of various polymer–graphene interfacial systems through atomistic molecular dynamics simulations, Soft Matter 10 (2014) 2876-2888.
- [57] A.N. Rissanou, V. Harmandaris, Structural and Dynamical Properties of Polystyrene Thin Films Supported by Multiple Graphene Layers, Macromolecules 48 (2015) 2761-2772.
- [58] A.P. Sgouros, G.G. Vogiatzis, G. Kritikos, A. Boziki, A. Nikolakopoulou, D. Liveris, D.N. Theodorou, Molecular Simulations of Free and Graphite Capped Polyethylene Films: Estimation of the Interfacial Free Energies, Macromolecues 50 (2017) 8827-8844.
- [59] A.F. Behbahani, S.M.V. Allaei, G.H. Motlagh, H. Eslami, V.A. Harmandaris, Structure, Dynamics, and Apparent Glass Transition of Stereoregular Poly(methyl methacrylate)/Graphene Interfaces through Atomistic Simulations, Macromolecules 2018 (2018) 7518-7532.
- [60] T. Koga, D. Barkley, M. Nagao, T. Taniguchi, J.M.Y. Carrillo, B.G. Sumpter, T. Masui, H. Kishimoto, M. Koga, J.G. Rudick, M.K. Endoh, Interphase Structures and Dynamics near Nanofiller Surfaces in Polymer Solutions, Macromolecules 51 (2018) 9462-9470.
- [61] A.S. Michaels, W.R. Vieth, H.H. Alcalay, The solubility parameter of polypropylene, J. Appl. Polym. Sci. 12 (1968) 1621-1624.
- [62] K. Wood, J. P. Mata, C. J. Garvey, C.-M. Wu, W. A. Hamilton, P. Abbeywick, D. Bartlett,

- F. Bartsch, P. Baxter, N. Booth, W. Brown, J. Christoforidis, D. Clowes, T. d'Adam, F. Darmann, M. Deura, S. Harrison, N. Hauser, G. Horton, D. Federici, F. Franceschini, P. Hanson, E. Imamovic, P. Imperia, M. Jones, S. Kennedy, S. Kim, T. Lam, W. T. Lee, M. Lesha, D. Mannicke, T. Noakes, S. R. Olsen, J. C. Osborn, D. Penny, M. Perry, S. A. Pullen, R. A. Robinson, J. C. Schulz, N. Xiong, E. P. Gilbert, QUOKKA, the pinhole small-angle neutron scattering instrument at the OPAL Research Reactor, Australia: design, performance, operation and scientific highlights, J. Appl. Cryst. 51 (2018) 294-314.
- [63] S.R. Kline, Reduction and analysis of SANS and USANS data using IGOR Pro, J Appl Crystallogr 39 (2006) 895-900.
- [64] K. Shibata, N. Takahashi, Y. Kawakita, M. Matsuura, T. Yamada, T. Tominaga, W. Kambara, M. Kobayashi, Y. Inamura, T. Nakatani, K.Nakajima, M. Arai, The Performance of TOF near Backscattering Spectrometer DNA in MLF, J-PARC, JPS Conf. Proc. 8 (2015) 036022.
- [65] R.T. Azuah, L.R. Kneller, Y. Qiu, P.L. Tregenna-Piggott, C.M. Brown, J.R. Copley, R.M. Dimeo, DAVE: A Comprehensive Software Suite for the Reduction, Visualization, and Analysis of Low Energy Neutron Spectroscopic Data, J. Res. Natl. Inst. Stand. Technol. 114 (2009) 341-58.
- [66] A.E. Tonelli, Conformational Characteristics of Isotactic Polypropylene, Macromolecules 5 (1972) 563-566.
- [67] R.W.G. Wyckoff, Crystal structures, 2nd edition ed.1963.
- [68] M.D. Hanwell, D.E. Curtis, D.C. Lonie, T. Vandermeersch, E. Zurek, G.R. Hutchison, Avogadro: an advanced semantic chemical editor, visualization, and analysis platform, J. Cheminform 4 (2012) 1-7.
- [69] J. Wang, R.M. Wolf, J.W. Caldwell, P.A. Kollman, D.A. Case, Development and testing of a general amber force field, J. Comput. Chem. 25 (2004) 1157-1174.
- [70] H.M.A. D.A. Case, K. Belfon, I.Y. Ben-Shalom, J.T. Berryman, S.R. Brozell, D.S. Cerutti, T.E. Cheatham, III, G.A. Cisneros, V.W.D. Cruzeiro, T.A. Darden, R.E. Duke, G. Giambasu, M.K. Gilson, H. Gohlke, A.W. Goetz, R. Harris, S. Izadi, S.A. Izmailov, K. Kasavajhala, M.C. Kaymak, E. King, A. Kovalenko, T. Kurtzman, T.S. Lee, S. LeGrand, P. Li, C. Lin, J. Liu, T.

- Luchko, R. Luo, M. Machado, V. Man, M. Manathunga, K.M. Merz, Y. Miao, O. Mikhailovskii, G. Monard, H. Nguyen, K.A. O'Hearn, A. Onufriev, F. Pan, S. Pantano, R. Qi, A. Rahnamoun, D.R. Roe, A. Roitberg, C. Sagui, S. Schott-Verdugo, A. Shajan, J. Shen, C.L. Simmerling, N.R. Skrynnikov, J. Smith, J. Swails, R.C. Walker, J Wang, J. Wang, H. Wei, R.M. Wolf, X. Wu, Y. Xiong, Y. Xue, D.M. York, S. Zhao, and P.A. Kollman Amber 2022, in: U.o. California (Ed.) San Francisco, 2022.
- [71] J.M. Martínez, L. Martínez, Packing optimization for automated generation of complex system's initial configurations for molecular dynamics and docking, J. Comput. Chem. 24 (2003) 819-825.
- [72] R.A. L. Martínez, E. G. Birgin, J. M. Martínez. Packmol, A package for building initial configurations for molecular dynamics simulations, J. Comput. Chem. 30 (2009) 2157-2164.
- [73] R.W. Hockney, J.W. Eastwood, Computer simulation using particles, CRC Press (1998).
- [74] B. Wunderlich, Thermal analysis of polymeric materials, Springer Science & Business Media (2005).
- [75] A.S. Nielsen, D. Batchelder, R. Pyrz, Estimation of crystallinity of isotactic polypropylene using Raman spectroscopy, Polymer 43 (2002) 2671-2676.
- [76] J.A. Torres, P.F. Nealey, J.J. de Pablo, Molecular Simulation of Ultrathin Polymeric Films near the Glass Transition, Phys. Rev. Lett. 85 (2000) 3221-3224.
- [77] A. Shavit, R.A. Riggleman, Physical Aging, the Local Dynamics of Glass-Forming Polymers under Nanoscale Confinement, J. Phys. Chem. B 118 (2014) 9096-9103.
- [78] W.L. Merling, J.B. Mileski, J.F. Douglas, D.S. Simmons, The Glass Transition of a Single Macromolecule, Macromolecules 49 (2016) 7597-7604.
- [79] W. Xia, J. Song, D.D. Hsu, S. Keten, Side-group size effects on interfaces and glass formation in supported polymer thin films, J. Chem. Phys. 146 (2017) 203311.
- [80] N. Jiang, M. Sen, M.K. Endoh, T. Koga, E. Langhammer, P. Bjöörn, M. Tsige, Thermal Properties and Segmental Dynamics of Polymer Melt Chains Adsorbed on Solid Surfaces, Langmuir 34 (2018) 4199-4209.
- [81] R.-D. Maier, R. Thomann, J. Kressler, R. Mulhaupt, B. Rudolf, The Influence of Stereoregularity on the Miscibility of Poly (propylene)s, J. Poly. Sci. B: Polym. Phys. 35 (1998)

- 1135-1144.
- [82] D. Richter, M. Monkenbusch, A. Arbe, J. Colmenero, Neutron scattering and the glass transition in polymers present status and future opportunities, J. Non-Cryst. Solids 287 (2001) 286–296.
- [83] D. Richter, M. Monkenbusch, A. Arbe, J. Colmenero, Neutron Spin Echo in Polymer Systems, Adv. Polym. Sci. 174 (2005) 1-221.
- [84] A. Arbe, J. Colmenero, M. Monkenbusch, D. Richter, Dynamics of Glass-Forming Polymers: "Homogeneous" versus "Heterogeneous" Scenario, Phys. Rev. Lett. 81 (1998) 590-593.
- [85] V. Arrighi, D. Batt-Coutrot, C. Zhang, M.T.F. Telling, A. Triolo, Effect of tacticity on the local dynamics of polypropylene melts, J. Chem. Phys. 119 (2003) 1271-1278.
- [86] M. Kaburagi, Y. Bin, D. Zhu, C. Xu, M. Matsuo, Small angle X-ray scattering from voids within fibers during the stabilization and carbonization stages, Carbon 41 (2003) 915-926.
- [87] J.S. Speck, M. Endo, M.S. Dresselhaus, Structure and intercalation of thin benzene derived carbon fibers, J. Cryst. Growth 94 (1989) 834–848.
- [88] C. Mark, O. Holderer, J. Allgaier, E. Hübner, W. Pyckhout-Hintzen, M. Zamponi, A. Radulescu, A. Feoktystov, M. Monkenbusch, N. Jalarvo, D. Richter, Polymer Chain Conformation and Dynamical Confinement in a Model One-Component Nanocomposite, Phy. Rev. Lett. 119 (2017) 047801.
- [89] J. Tanchawanich, V. Arrighi, M.C. Sacchi, M.T. Telling, A. Triolo, Fast and slow dynamics of isotactic polypropylene melts, Macromolecules 26 (2008) 1560-1564.
- [90] A. Arbe, J. Colmenero, F. Alvarez, M. Monkenbusch, D. Richter, B. Farago, B. Frick, Non-Gaussian Nature of the α Relaxation of Glass-Forming Polyisoprene, Phys. Rev. Lett. 89 (2002) 245701.
- [91] A. Arbe, J. Colmenero, F. Alvarez, M. Monkenbusch, D. Richter, B. Farago, B. Frick, Experimental evidence by neutron scattering of a crossover from Gaussian to non-Gaussian behavior in the α relaxation of polyisoprene, Phys. Rev. E 67 (2003) 051802.
- [92] M. Krutyeva, J. Martin, A. Arbe, J. Colmenero, C. Mijangos, G.J. Schneider, T. Unruh, Y. Su, D. Richter, Neutron scattering study of the dynamics of a polymer melt under nanoscopic

- confinement J. Chem. Phys. 131 (2009) 174901.
- [93] J.H. Roh, M. Tyagi, T.E. Hogan, C.M. Roland, Space-Dependent Dynamics in 1,4-Polybutadiene Nanocomposite, Macromolecules 46 (2013) 6667-6669.
- [94] O. Ahumada, D.N. Theodorou, A. Triolo, V. Arrighi, C. Karatasos, J.-P. Ryckaert, Segmental Dynamics of Atactic Polypropylene As Revealed by Molecular Simulations and Quasielastic Neutron Scattering, Macromolecules 35 (2002) 7110-7124.
- [95] A. Opdahl, R.A. Phillips, G.A. Somorjai, Effect of Bulk Miscibility on the Surface Composition of Polypropylene/Poly(ethylene-co-propylene) Blends, Macromolecules 35 (2002) 4387-4396.
- [96] D. Kawaguchi, K. Yamamoto, T. Abe, N. Jiang, T. Koga, S. Yamamoto, K. Tanaka, Local orientation of chains at crystal/amorphous interfaces buried in isotactic polypropylene thin films, Phys. Chem. Chem. Phys. 23 (2021) 23466-23472.
- [97] J.M.Y. Carrillo, S.W. Cheng, R. Kumar, M. Goswami, A.P. Sokolov, B.G. Sumpter, Untangling the Effects of Chain Rigidity on the Structure and Dynamics of Strongly Adsorbed Polymer Melts, Macromolecules 48 (2015) 4207-4219.
- [98] M. Sen, N. Jiang, J. Cheung, M.K. Endoh, T. Koga, D. Kawaguchi, K. Tanaka, Flattening Process of Polymer Chains Irreversibly Adsorbed on a Solid, ACS Macro Lett. 5 (2016) 504-508.
- [99] N. Jiang, J. Shang, X. Di, M.K. Endoh, T. Koga, Formation Mechanism of High-Density, Flattened Polymer Nanolayers Adsorbed on Planar Solids, Macromolecules 47 (2014) 2682-2689.
- [100] M.D. Ediger, J.A. Forrest, Dynamics near Free Surfaces and the Glass Transition in Thin Polymer Films: A View to the Future, Macromolecules 47 (2014) 471-478.
- [101] C.B. Roth, K.L. McNerny, W.F. Jager, J.M. Torkelson, Eliminating the enhanced mobility at the free surface of polystyrene: Fluorescence studies of the glass transition temperature in thin bilayer films of immiscible polymers, Macromolecules 40 (2007) 2568–2574.
- [102] B. Zuo, H. Zhou, M.J.B. Davis, X. Wang, R.D. Priestley, Effect of Local Chain Conformation in Adsorbed Nanolayers on Confined Polymer Molecular Mobility, Phys. Rev. Lett. 122 (2019) 217801.